International Journal of
Molecular Sciences

MDPI

Article

Prediction of Strong Transversal s(TE) Exciton–Polaritons in C_{60} Thin Crystalline Films

Vito Despoja [1,2,*] and Leonardo Marušić [3]

[1] Institut za Fiziku, Bijenička 46, 10000 Zagreb, Croatia
[2] Donostia International Physics Center (DIPC), P. Manuel de Lardizabal, 4, 20018 San Sebastián, Spain
[3] Maritime Department, University of Zadar, M. Pavlinovića 1, 23000 Zadar, Croatia; lmarusic@unizd.hr
* Correspondence: vito@phy.hr

Abstract: If an exciton and a photon can change each other's properties, indicating that the regime of their strong bond is achieved, it usually happens in standard microcavity devices, where the large overlap between the 'confined' cavity photons and the 2D excitons enable the hybridization and the band gap opening in the parabolic photonic branch (as clear evidence of the strong exciton–photon coupling). Here, we show that the strong light–matter coupling can occur beyond the microcavity device setup, i.e., between the 'free' s(TE) photons and excitons. The s(TE) exciton–polariton is a polarization mode, which (contrary to the p(TM) mode) appears only as a coexistence of a photon and an exciton, i.e., it vanishes in the non-retarded limit ($c \to \infty$). We show that a thin fullerene C_{60} crystalline film (consisting of N C_{60} single layers) deposited on an Al_2O_3 dielectric surface supports strong evanescent s(TE)-polarized exciton–polariton. The calculated Rabi splitting is more than $\Omega = 500$ meV for $N = 10$, with a tendency to increase with N, indicating a very strong photonic character of the exciton–polariton.

Keywords: eksciton-polaritons; molecular crystals; optical conductivity; photonics

Citation: Despoja, V.; Marušić, L. Prediction of Strong Transversal s(TE) Exciton–Polaritons in C_{60} Thin Crystalline Films. *Int. J. Mol. Sci.* **2022**, *23*, 6943. https://doi.org/10.3390/ijms23136943

Academic Editor: Ana María Díez-Pascual

Received: 24 May 2022
Accepted: 20 June 2022
Published: 22 June 2022

1. Introduction

The interaction between photons and polarization modes can result in the formation of hybrid photon polarization modes, called polaritons [1]. Very common platforms for studying strong light–matter interactions are the gapped systems, such as semiconductors [2,3] or molecules [4], placed in microcavity devices, where the cavity exciton–polaritons are formed. The quantum nature of a cavity exciton–polariton manifests in the form of the Bose–Einstein condensation, which has recently been experimentally detected [2,5,6]. The cavity exciton–polaritons are routinely observed in bulk [7–10] and quantum well systems [3,11], e.g., devised from GaAs [3]. Two-dimensional (2D) materials, such as semiconducting monolayers, thin heterostructures, and films, are even more attractive than their bulk counterparts, due to the reduced Coulomb screening and the corresponding large exciton binding energies [12–19] that enable the formation of well-defined exciton–polaritons even at room temperatures [20]. The first 2D exciton–polaritons were obtained in a monolayer of a transition metal dichalcogenide (TMD) MoS_2, where the Rabi splitting between the exciton and the cavity photon of ∼50 meV was observed [21]. Further photoluminescence studies showed clear anti-crossing behavior and splitting of the exciton–polariton in other 2D TMD cavity devices, e.g., in $MoSe_2$ [22], WS_2 [23], WSe_2 [24,25], and in the $MoSe_2$-WSe_2 heterostructure [26]. In addition, the real-space imaging of the exciton–polaritons has been done by means of near-field scanning optical microscopy for WSe_2 thin films [27]. Finally, a remarkable Rabi splitting of 440 meV was theoretically predicted in the monolayer hexagonal boron nitride cavity device [28], suggesting extraordinary strong light–matter interaction in 2D heterostructures.

The strongest exciton–photon coupling is achieved in the organic dye molecule thin films placed in a microcavity [29]. For example, Rabi splitting of $\Omega \leq 450$ meV [30–32],

0.7 eV [33], and even more than 1 eV [34,35] have been detected when various organic dye molecules were placed in a planar microcavity. The theoretical approach to such systems is mostly based on the two-level or boson–boson Hamiltonian model with an arbitrary coupling constant [4,36]. Using graphene [37] or perovskite [38]-layered heterostructures, one can obtain tunable microcavity devices of high performance, which can be applied as photonic detectors or emitters [38,39], but also as platforms for studying the exciton–photon coupling.

All these studies use the same concept: an exciton in a semiconducting nanostructure hybridizes with a photon 'confined' in a metallic microcavity. Such cavity photons and excitons are expected to interact stronger as the photon is more confined (i.e., the overlap between the exciton and photon is larger) and as the exciton oscillator strength [28] is larger. In this paper, we change the concept and explore the coupling between the 'free' photons and the excitons in the 2D nanostructures. The coupling between the 'free' photons and the polarization modes (such as plasmons, phonons, or excitons at surfaces or in 2D nanostructures) is a well-known, widely explored phenomenon [40–47]. The inherent property of all these eigenmodes (called plasmon polaritons, phonon polaritons, or exciton–polaritons) is their evanescent character, i.e., they are well-defined eigenmodes with the electromagnetic field (wave function) strongly localized at the interface or within the 2D nanostructure. Moreover, these modes usually have p or transverse-magnetic (TM) polarization, i.e., the electric field (and, therefore, the currents as well) has a component parallel to the direction of propagation. The most relevant point is that the p(TM) polarized plasmon polariton, phonon polariton, or exciton–polariton branches reduce to the plasmon, phonon, or exciton branches in the non-retarded ($c \to \infty$) limit. On the other hand, the electric field and the current of s or transverse-electric (TE) electromagnetic eigenmodes are perpendicular to the direction of their propagation. An especially attractive aspect of these polarization modes is that they **do not** exist in the non-retarded ($c \to \infty$) limit, i.e., they appear only as the coexistence of a photon and an exciton. The extent of the photon's participation in the s(TE) exciton–polariton is determined from the bending of the horizontal exciton branch (ω_{ex}) at the exciton–photon crossing ($\omega_{ex} = Q_{ex}c/\sqrt{\epsilon}$, where Q_{ex} is the photon wave vector at the exciton–photon crossing point), which we call the Rabi splitting Ω, to keep the terminology compatible with the cavity systems. Even though the s(TE) surface or 2D polaritons do exist [40] for some conditions, there is still no experimental evidence of such modes. However, the hybridization between the s(TE) Bloch surface waves (BSWs) (i.e., the photons confined between a truncated photonic crystal and a semi-infinite dielectric), and the excitons has been experimentally demonstrated in both inorganic (quantum well and TMD monolayer) and organic systems [48–51].

We show that very strong s(TE) exciton–polaritons may occur in layered van der Waals (vdW) heterostructures. The prototypical layered nanostructure we investigate in this paper is a thin film of the FCC fullerite (crystalline fullerene) cut along the (111) planes so that it formed several (N) molecular (C_{60}) layers. The crystalline C_{60} films were also deposited on a dielectric Al_2O_3 surface to make the simulation more realistic. The epitaxial growth of the C_{60} thin films of various thicknesses on various metallic or dielectric substrates under ambient conditions and in high vacuum was studied in references [52–58]. Some experimental studies even show that the crystalline growth of the C_{60} thin films on pentacene buffer layers is exclusively (111)-oriented [55]. Theoretical, molecular dynamic simulations of the C_{60} multilayer epitaxial growth and stability on various substrates were investigated in references [58–61]. These experimental/theoretical studies suggest that our model system is indeed highly realistic.

In this paper, the light–matter interaction was studied using our quantum electrodynamic Bethe–Salpeter equation approach (QE-BSE) developed in references [28,47]. This approach describes both excitons and photons by bosonic propagators σ and Γ, respectively, derived from the first principles. The C_{60} optical conductivity σ was calculated using *ab initio* G_0W_0-BSE method [47,62], and the free proton propagator Γ was derived by solving Maxwell's equation at the vacuum/dielectric interface [63,64]. The dielectric surface was

described by the local dielectric function $\epsilon_M(\omega)$, also determined from the first principles. The exciton–photon coupling was achieved by dressing the free-photon propagator Γ with excitons at the random phase approximation (RPA) level. We studied the s(TE)-polarized exciton–polariton in the C_{60} thin crystalline film as a function of the number N of the C_{60} single layers. We obtained a very strong hybridization between the exciton in the C_{60} thin film and the s(TE) free photons. The hybridization increased with N, and for $N = 10$, we achieved the Rabi splitting Ω even larger than 1000 meV and 500 meV for self-standing and supported C_{60} films, respectively.

The paper is organized as follows. In Section 2, we present the geometry of the system and the derivation of the optical conductivity $\tilde{\sigma}$ of the C_{60} single layer using the G_0W_0-BSE approach with the solution of Dyson's equation for the electric field propagator $\mathcal{E} = \Gamma + \Gamma\tilde{\sigma}\mathcal{E}$. In Section 3, we present the spectra of the electromagnetic modes $S = \mathrm{Re}\mathcal{E}$, as well as the dispersion relations and intensities of the s(TE)-polarized exciton–polaritons in the C_{60} thin films of different thicknesses N, in vacuum, and at a Al_2O_3 surface. The conclusions are presented in Section 4.

2. Theoretical Formulation

We assume the the C_{60} molecules, upon deposition on the crystal surface, self-assemble in a regular FCC structure (the most stable bulk structure of crystalline fullerene) forming a (111) surface, as shown in Figure 1a. The FCC crystal lattice constant is taken to be $a_{3D} = 14$ Å [61], and the separation between the layers is fixed to be $\Delta = a_{3D}/\sqrt{3} = 8.1$ Å. Each crystal plane forms a 2D hexagonal Bravais lattice with the lattice constant $a_{2D} = a_{3D}/\sqrt{2} = 9.9$ Å, as shown in Figure 1b. The C_{60} films, occupying $z > 0$ half-space, are immersed in a dielectric medium described by a dielectric constant ϵ_0. The dielectric response of the substrate, occupying $z < 0$ half-space, is approximated by a local macroscopic dielectric function $\epsilon_M(\omega)$.

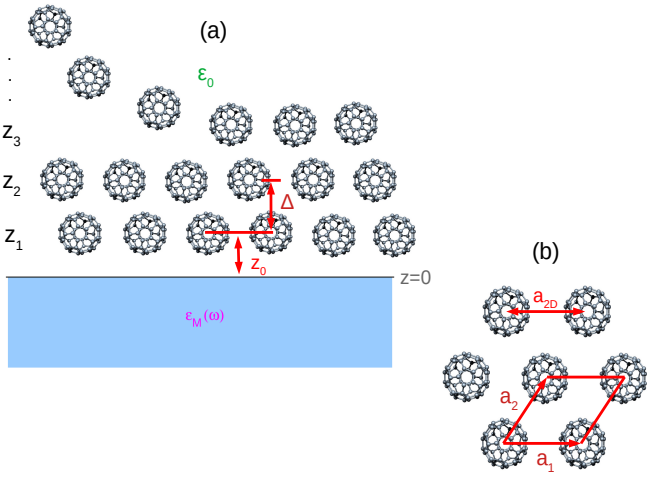

Figure 1. (**a**) C_{60} molecules upon deposition on the surface self-assemble in a regular FCC structure forming a (111) surface. The C_{60} layers, occupying $z > 0$ half-space, are immersed in a dielectric medium described by a dielectric constant ϵ_0. The dielectric response of the substrate, occupying $z < 0$ half-space, is approximated by a local macroscopic dielectric function $\epsilon_M(\omega)$. The FCC lattice constant is $a_{3D} = 14$ Å so that the separation between the layers is $\Delta = a_{3D}/\sqrt{3} = 8.1$ Å. (**b**) Each crystal plane forms a 2D-hexagonal Bravais lattice with lattice constant $a_{2D} = a_{3D}/\sqrt{2} = 9.9$ Å.

2.1. Calculation of Electric Field Propagator $\mathcal{E}$

The quantity we used to extract the information from the electromagnetic modes in the C_{60} films deposited on a dielectric surface was the electric field propagator $\mathcal{E}_{\mu\nu}$, which

provides the electric field produced by an external oscillating point dipole $\mathbf{p}_0 e^{-i\omega t}$ placed at point $\mathbf{r}'$ as [63,64]

$$E_\mu(\mathbf{r},\omega) = \sum_{\nu=x,y,z} \mathcal{E}_{\mu\nu}(\mathbf{r},\mathbf{r}',\omega) p_\nu^0. \tag{1}$$

The propagator $\mathcal{E}$ is the solution of Dyson's equation [28,47,64,65]

$$\mathcal{E}_{\mu\nu}(\mathbf{r},\mathbf{r}',\omega) = \Gamma_{\mu\nu}(\mathbf{r},\mathbf{r}',\omega) + \sum_{\alpha,\beta=x,y,z} \int d\mathbf{r}_1 \int d\mathbf{r}_2 \, \Gamma_{\mu\alpha}(\mathbf{r},\mathbf{r}_1,\omega)\sigma_{\alpha\beta}(\mathbf{r}_1,\mathbf{r}_2,\omega)\mathcal{E}_{\beta\nu}(\mathbf{r}_2,\mathbf{r}',\omega), \tag{2}$$

where the integration is performed over the entire space, σ is the nonlocal conductivity tensor of the deposited C_{60} thin film, and Γ is the electric field propagator in the absence of the C_{60} film, i.e., when $\sigma = 0$ [64,65]. The propagator Γ also includes the electromagnetic field scattering at the medium/substrate interface. If each molecule is approximated as a point polarizable dipole, then the optical conductivity of the C_{60} film can be written as

$$\sigma_{\mu\nu}(\mathbf{r},\mathbf{r}',\omega) = \sum_{i=1}^{N} \sum_{\mathbf{R}_\parallel} \sigma_i^{\mu\nu}(\omega)\delta(\boldsymbol{\rho} - \mathbf{R}_\parallel)\delta(z - z_i)\delta(\boldsymbol{\rho}' - \mathbf{R}_\parallel)\delta(z' - z_i), \tag{3}$$

where $\sigma_i^{\mu\nu}(\omega)$ is the optical conductivity tensor of a single molecule in the i-th molecular layer. This approximation is fully justified in the optical limit $2\pi c/\omega_{\text{light}} >> R_{\text{M}}$, where R_{M} is the radius of a C_{60} molecule. Note that although all the molecules are equal, we distinguished between their conductivities in different layers $\sigma_i; i = 1, N$, due to the different influences of the substrates on a molecule in a different layer. The 2D Bravais lattice translation vectors spanning the molecular crystal are

$$\mathbf{R}_\parallel = n\mathbf{a}_1 + m\mathbf{a}_2; \;\; n, m \in \mathbb{Z}, \tag{4}$$

where $\mathbf{a}_1$ and $\mathbf{a}_1$ are the primitive vectors, as illustrated in Figure 1b. The molecular layers occupy the planes

$$z_i = z_0, z_0 + \Delta, z_0 + 2\Delta, \ldots, z_0 + (N-1)\Delta,$$

where N is the number of molecular layers. Due to the planar translational invariance of the substrate, the Fourier transform of the propagator Γ is

$$\Gamma_{\mu\nu}(\mathbf{r},\mathbf{r}',\omega) = \int \frac{d\mathbf{Q}}{(2\pi)^2} \Gamma_{\mu\nu}(\mathbf{Q},\omega,z,z') e^{i\mathbf{Q}(\boldsymbol{\rho}-\boldsymbol{\rho}')}, \tag{5}$$

where $\mathbf{Q} = (Q_x, Q_x)$ are the two-dimensional wave vectors. The propagator $\mathcal{E}$ should also include the effects of the electromagnetic field Bragg scattering at the 2D crystal lattice, so that its Fourier transform is

$$\mathcal{E}_{\mu\nu}(\mathbf{r},\mathbf{r}',\omega) = \sum_{\mathbf{g}_\parallel} \int \frac{d\mathbf{Q}}{(2\pi)^2} \mathcal{E}_{\mathbf{g}_\parallel}^{\mu\nu}(\mathbf{Q},\omega,z,z') e^{i\mathbf{Q}\boldsymbol{\rho}} e^{-i(\mathbf{Q}+\mathbf{g}_\parallel)\boldsymbol{\rho}'}, \tag{6}$$

where

$$\mathbf{g}_\parallel = n\mathbf{b}_1 + m\mathbf{b}_2; \;\; n, m \in \mathbb{Z} \tag{7}$$

are 2D reciprocal vectors, while $\mathbf{b}_1$ and $\mathbf{b}_1$ are primitive reciprocal vectors. After inserting (3), (5), and (6) in (2), it becomes an equation in the $(\mathbf{Q},\omega,z)$ space

$$\mathcal{E}_{\mathbf{g}_\parallel}^{\mu\nu}(\mathbf{Q},\omega,z,z') = \Gamma_{\mu\nu}(\mathbf{Q},\omega,z,z') + \sum_{\alpha,\beta=x,y,z} \sum_i \sum_{\mathbf{g}'_\parallel} \Gamma_{\mu\alpha}(\mathbf{Q},\omega,z,z_i)\tilde{\sigma}_i^{\alpha\beta}(\omega)\mathcal{E}_{\mathbf{g}_\parallel+\mathbf{g}'_\parallel}^{\beta\nu}(\mathbf{Q}-\mathbf{g}'_\parallel,\omega,z_i,z'), \tag{8}$$

where the surface optical conductivity is

$$\tilde{\sigma}_i^{\alpha\beta}(\omega) = \frac{1}{S_{\text{fcc}}}\sigma_i^{\alpha\beta}(\omega), \tag{9}$$

and $S_{\text{fcc}} = (\mathbf{a}_1 \times \mathbf{a}_2)\hat{\mathbf{z}} = a_{\text{2D}}^2\sqrt{3}/2$ is the area of the 2D unit cell. If we neglect the electromagnetic field Bragg scattering, by introducing $\mathbf{g}_\parallel = \mathbf{g}'_\parallel = 0$ in Equation (8), and inserting $z = z_i$ and $z' = z_j$, the equation becomes the matrix tensor equation:

$$\mathcal{E}_{\mu\nu}(\mathbf{Q},\omega,z_i,z_j) = \Gamma_{\mu\nu}(\mathbf{Q},\omega,z_i,z_j) + \sum_{\alpha,\beta=x,y,z}\sum_k \Gamma_{\mu\alpha}(\mathbf{Q},\omega,z_i,z_k)\tilde{\sigma}_k^{\alpha\beta}(\omega)\mathcal{E}_{\beta\nu}(\mathbf{Q},\omega,z_k,z_j), \tag{10}$$

where $\mathcal{E}^{\mu\nu}(z_i,z_j)$ is the electric field propagator within ($i = j$) or between ($i \neq j$) the C_{60} layers. The electrical field propagator in the absence of the C_{60} film can be written as

$$\mathbf{\Gamma} = \mathbf{\Gamma}^0 + \mathbf{\Gamma}^{sc}, \tag{11}$$

where the propagator of the 'free' electric field (or free photons propagator) is [63,64]

$$\mathbf{\Gamma}^0(\mathbf{Q},\omega,z,z') = -\frac{4\pi i}{\epsilon_0\omega}\delta(z-z')\mathbf{z}\cdot\mathbf{z} - \frac{2\pi\omega}{\beta_0 c^2}e^{i\beta_0|z-z'|}\sum_{q=s,p}\mathbf{e}_q^0\cdot\mathbf{e}_q^0. \tag{12}$$

The propagator of the scattered electric field in the region $z, z' > 0$ is [63]

$$\mathbf{\Gamma}^{\text{sc}}(\mathbf{Q},\omega,z,z') = -\frac{2\pi\omega}{\beta_0 c^2}e^{i\beta_0(z+z')}\sum_{q=s,p} r_q\cdot\mathbf{e}_q^+\cdot\mathbf{e}_q^-. \tag{13}$$

Here, the unit vectors of the s(TE)-polarized electromagnetic field are

$$\mathbf{e}_s^{0,\pm} = \mathbf{Q}_0 \times \mathbf{z}.$$

and the unit vectors of the p(TM) polarized electromagnetic field are

$$\mathbf{e}_p^{0,\pm} = \frac{c}{\omega\sqrt{\epsilon_0}}[\alpha_{0,\pm}\beta_0\mathbf{Q}_0 + Q\mathbf{z}],$$

where $\alpha_0 = -sgn(z-z')$, $\alpha_\pm = \mp 1$, and $\mathbf{Q}_0$ and $\mathbf{z}$ are the unit vectors in the $\mathbf{Q}$ and z directions, respectively. The reflection coefficients of the s(TE) and p(TM) polarized electromagnetic waves at the medium/substrate interface are

$$r_s = \frac{\beta_0 - \beta_{\text{M}}}{\beta_0 + \beta_{\text{M}}}$$

and

$$r_p = \frac{\beta_0\epsilon_{\text{M}} - \beta_{\text{M}}\epsilon_0}{\beta_0\epsilon_{\text{M}} + \beta_{\text{M}}\epsilon_0},$$

respectively, and the complex wave vectors in perpendicular (z) direction are

$$\beta_{0,\text{M}} = \sqrt{\frac{\omega^2}{c^2}\epsilon_{0,\text{M}}(\omega) - |\mathbf{Q}|^2}.$$

The β_0 and β_{M} determine the character of the electromagnetic modes at the medium/dielectric substrate interface. To simplify the interpretation, we assume that the dielectric medium is vacuum, i.e., $\epsilon_0 = 1$, and that the dielectric function of the substrate is constant $\epsilon_{\text{M}}(\omega) = \epsilon_{\text{M}}$, which is a plausible approximation for many wide band gap insulators. In the vacuum, for $\omega > Qc$, β_0 is a real number; therefore, the electromagnetic modes have a radiative character, and for $\omega < Qc$, β_0 is an imaginary number so that the electromagnetic modes have evanescent character. The two regions are separated by the so-called 'light-line'

$\omega = Qc$, as illustrated by the magenta line in Figure 2a. In analogy to that, the two regions in the substrate are separated by the $\omega = Qc/\sqrt{\epsilon_M}$ line, as illustrated by the green line in Figure 2a. Since $\epsilon_M > 1$, the slope of the light-line in the substrate is smaller than in the vacuum, so in the gap $Qc/\sqrt{\epsilon_M} < \omega < Qc$, the light propagates freely into the substrate but has an evanescent character in the vacuum region, as illustrated in Figure 2a. Therefore, the exciton–polariton mode $\omega_{\text{ex-pol}}$ is expected to appear in the fully evanescent region $\omega < Qc/\sqrt{\epsilon_M}$, since in that region it cannot be irradiated into the surrounding media. The evanescent character of the electric field produced by the exciton–polariton in the C_{60} film is illustrated in Figure 2b.

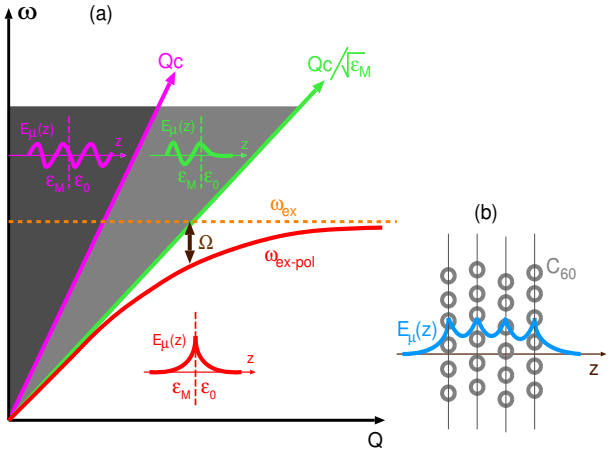

Figure 2. (**a**) The character of the electromagnetic modes at the dielectric/vacuum (ϵ_M/ϵ_0) interface. In the region $\omega > Qc$, the electromagnetic modes are entirely radiative (both in vacuum and in the dielectric), in the region $Qc/\sqrt{\epsilon_M} < \omega < Qc$, they are radiative in the dielectric and evanescent in vacuum, and in the $\omega < Qc/\sqrt{\epsilon_M}$ region, they have fully evanescent character. In the latter region, the photon and molecular exciton (ω_{ex}) hybridize, and an exciton–polariton ($\omega_{\text{ex-pol}}$) occurs. The measure of the coupling strength between the exciton ω_{ex} and the photon is given by Rabi splitting Ω. (**b**) The evanescent electric field $E_\mu(z)$ produced by an exciton–polariton in the C_{60} film.

We chose the electromagnetic modes to propagate in the $\mathbf{Q}_0 = \mathbf{y}$ directions. In this case, the Dyson Equation (10) decouples into the independent matrix and the matrix tensor equations for the s(TE) and p(TM) polarizations, respectively. Here, we explore the s(TE)-polarized electromagnetic modes, which satisfy the matrix equation:

$$\mathcal{E}_{xx}(|\mathbf{Q}|\mathbf{y},\omega,z_i,z_j) = \Gamma_{xx}(|\mathbf{Q}|\mathbf{y},\omega,z_i,z_j) + \sum_k \Gamma_{xx}(|\mathbf{Q}|\mathbf{y},\omega,z_i,z_k)\tilde{\sigma}_k^{xx}(\omega)\mathcal{E}_{xx}(|\mathbf{Q}|\mathbf{y},\omega,z_k,z_j), \tag{14}$$

where after using (11)–(13)

$$\Gamma_{xx}(|\mathbf{Q}|\mathbf{y},\omega,z_i,z_j) = -\frac{2\pi\omega}{\beta_0 c^2}\left[e^{i\beta_0|z_i-z_j|} + r_s e^{i\beta_0(z_i+z_j)}\right]. \tag{15}$$

The first term in (15) represents the incident electromagnetic field, while the second term represents the one reflected at the vacuum/substrate boundary. In the electrostatic or non-retarded limit $c \to \infty$ and

$$\lim_{c\to\infty} \Gamma_{xx}(|\mathbf{Q}|\mathbf{y},\omega,z_i,z_j) = 0, \tag{16}$$

so that all the properties presented below are a direct consequence of the binding between the s(TE)-polarized light (photons) and the molecular excitons, and they vanish, i.e., do not exist in the electrostatic limit.

2.2. Calculation of the Optical Conductivity of a Single Molecule

First, we explain the calculation of the molecular conductivity $\sigma_i^{\mu\nu}(\omega)$ in a 'self-standing molecule'($z_0 \to \infty$), and then we extend that to the case when the molecule is close to a dielectric surface, i.e., when z_0 is finite, and chosen to be a characteristic vdW distance. The basic ingredients we need to calculate the molecular conductivity $\sigma_{\mu\nu}(\omega)$ are the molecular orbitals $\phi_n(\mathbf{r})$ and the energies E_n, which can be obtained by solving the Kohn–Sham equation self-consistently. We assume that the molecules are periodically repeating so that they form a simple cubic (sc) Bravais lattice with the unit cell a and volume $\Omega_{\rm sc} = a^3$. The unit cell a is chosen so that there is no intermolecular overlap. This allows the molecular states $|\phi_n\rangle$ to be calculated at the Γ point only. It should be emphasized that the sc lattice and the unit cell a are not related to the previously described FCC lattice with the unit cell '$a_{\rm 3D}$'. The purpose of the sc lattice is only to determine the molecular states $|\phi_n\rangle$ at the Γ point using the plane-wave DFT code. From now on, the conductivity of the 3D molecular crystal will be denoted as $\sigma_{\mu\nu}^{\rm 3D}(\omega)$.

The nonlocal optical conductivity tensor in the 3D molecular crystal is [62,64–66]

$$\sigma_{\mu\nu}^{\rm 3D}(\mathbf{r},\mathbf{r}',\omega) = \frac{2i}{\omega}\sum_{nm}\sum_{n'm'} \mathcal{K}_{n\to n'}^{m\leftarrow m'}(\omega) j_{nm}^{\mu}(\mathbf{r})[j_{n'm'}^{\nu}(\mathbf{r}')]^*, \tag{17}$$

where

$$j_{nm}^{\alpha}(\mathbf{r}) = \frac{e\hbar}{2im}\{\phi_n^*(\mathbf{r})\partial_\alpha\phi_m(\mathbf{r}) - [\partial_\alpha\phi_n^*(\mathbf{r})]\phi_m(\mathbf{r})\} \tag{18}$$

represents the current produced by the transition between the molecular states $|\phi_n\rangle \to |\phi_m\rangle$. Considering that the Bloch wave functions at the Γ point ϕ_n are periodic functions, tensor (17) can be expanded in the Fourier series

$$\sigma_{\mu\nu}^{\rm 3D}(\mathbf{r},\mathbf{r}',\omega) = \frac{1}{\Omega_{\rm sc}}\sum_{\mathbf{G}\mathbf{G}'} e^{i\mathbf{G}\mathbf{r}} e^{-i\mathbf{G}'\mathbf{r}'}\sigma_{\mathbf{G}\mathbf{G}'}^{\mu\nu}(\omega), \tag{19}$$

where the Fourier coefficients are

$$\sigma_{\mathbf{G}\mathbf{G}'}^{\mu\nu,\rm 3D}(\omega) = \frac{i}{\omega}\frac{2}{\Omega_{\rm sc}}\sum_{nm}\sum_{n'm'} j_{nm}^{\mu}(\mathbf{G})\mathcal{K}_{n\to n'}^{m\leftarrow m'}(\omega)[j_{n'm'}^{\nu}(\mathbf{G}')]^*, \tag{20}$$

and the current vertices are

$$j_{nm}^{\alpha}(\mathbf{G}) = \int_{\Omega_{\rm sc}} d\mathbf{r} e^{-i\mathbf{G}\mathbf{r}}\, j_{nm}^{\alpha}(\mathbf{r}). \tag{21}$$

The four-point polarizability $\mathcal{K}$ can be obtained by solving the Bethe–Salpeter (BS) equation [28,47]

$$\mathcal{K}_{n\to n'}^{m\leftarrow m'}(\omega) = \mathcal{L}_{n\to n'}^{m\leftarrow m'}(\omega) + \sum_{n_1m_1}\sum_{n_2m_2}\mathcal{L}_{n\to n_1}^{m\leftarrow m_1}(\omega)\,\Xi_{n_1\to n_2}^{m_1\leftarrow m_2}\,\mathcal{L}_{n_2\to n'}^{m_2\leftarrow m'}(\omega), \tag{22}$$

where the time-ordered electron–hole propagator is defined as

$$\mathcal{L}_{n\to n'}^{m\leftarrow m'}(\omega) = \delta_{nn'}\delta_{mm'}\int_{-\infty}^{\infty}\frac{d\omega'}{2\pi i}G_n(\omega')G_m(\omega+\omega'). \tag{23}$$

The propagator (or Green's function) of an electron or a hole in a molecular state $|\phi_n\rangle$ is

$$G_n(\omega) = \frac{1}{\omega - E_n + E_n^{\rm XC} - \Sigma_n^{\rm X} - \Sigma_n^{\rm C,0}(\omega)}, \tag{24}$$

where the exchange of self-energy is

$$\Sigma_n^{\rm X} = -\frac{1}{\Omega_{\rm sc}}\sum_m f_m \sum_{\mathbf{G}\mathbf{G}'}\rho_{nm}^*(\mathbf{G})V_{\mathbf{G}\mathbf{G}'}^{\rm C}(\mathbf{Q})\rho_{nm}(\mathbf{G}'). \tag{25}$$

The correlation self-energy in the G_0W_0 approximation is

$$\Sigma_n^{C,0}(\omega) = \frac{1}{\Omega_{sc}} \sum_m \sum_{\mathbf{GG'}} \rho^*_{nm}(\mathbf{G}) \rho_{nm}(\mathbf{G'}) \Big\{ (1 - f_m)\, \Gamma^0_{\mathbf{GG'}}(\omega - E_m) - f_m\, \Gamma^0_{\mathbf{GG'}}(E_m - \omega) \Big\}, \tag{26}$$

where the correlation propagator is defined as

$$\Gamma^0_{\mathbf{GG'}}(\omega) = \int_0^\infty d\omega' \frac{S^0_{\mathbf{GG'}}(\omega')}{\omega - \omega' + i\delta}, \tag{27}$$

and $f_n = \theta(E_F - E_n)$ is the Fermi–Dirac distribution at $T = 0$. The spectrum of the electronic excitation in a self-standing molecule is

$$S^0_{\mathbf{GG'}}(\omega) = -\frac{1}{\pi} Im W^0_{\mathbf{GG'}}(\omega). \tag{28}$$

To avoid double-counting, we excluded the DFT exchange–correlation contribution E_n^{XC} from the KS energy E_n in Equation (24). In the quasi-particle (QP) approximation, the electrons and holes have energies E_n^{QP}, which are the real poles of Green's function (24), i.e., they satisfy the equation

$$E_n - E_n^{XC} + \Sigma_n^X + Re\Sigma_n^{C,0}(E_n^{QP}) = E_n^{QP}. \tag{29}$$

The electron/hole Green functions can now be approximated as

$$G_n^{QP}(\omega) = \frac{1 - f_n^{QP}}{\omega - E_n^{QP} + i\delta} + \frac{f_n^{QP}}{\omega - E_n^{QP} - i\delta}, \tag{30}$$

and after they are used in (23), the time-ordered electron–hole propagator becomes

$$\mathcal{L}^{m \leftarrow m'}_{n \to n'}(\omega) = \frac{f_n^{QP} - f_m^{QP}}{\omega + E_n^{QP} - E_m^{QP} + i\delta sgn(E_m^{QP} - E_n^{QP})} \delta_{nn'} \delta_{mm'}, \tag{31}$$

where $\delta = 0^+$. The 'time-ordered' screened Coulomb interaction is the solution of Dyson's equation

$$W^0_{\mathbf{GG'}}(\omega) = V^C_{\mathbf{GG'}} + \sum_{\mathbf{G_1 G_2}} V^C_{\mathbf{GG_1}} \chi^0_{\mathbf{G_1 G_2}}(\omega) W^0_{\mathbf{G_2 G'}}(\omega), \tag{32}$$

where the matrix of the 'time-ordered' irreducible polarizability is

$$\chi^0_{\mathbf{GG'}}(\omega) = \frac{2}{\Omega_{sc}} \sum_{nm} \frac{(f_n - f_m)\rho_{nm}(\mathbf{G})\, \rho^*_{nm}(\mathbf{G'})}{\hbar\omega + E_n - E_m + i\delta sgn(E_m - E_n)}, \tag{33}$$

and the charge vertices are

$$\rho_{nm}(\mathbf{G}) = \int_{\Omega_{sc}} d\mathbf{r}\, \phi^*_n(\mathbf{r}) e^{-i\mathbf{G}\mathbf{r}} \phi_m(\mathbf{r}). \tag{34}$$

Since we calculate the optical conductivity of a single isolated benzene molecule, we have to exclude the effect on its polarizability due to the interaction with the surrounding molecules in the sc lattice. This is accomplished by using the truncated Coulomb interaction [67]

$$V_C(\mathbf{r} - \mathbf{r'}) = \frac{\Theta(|\mathbf{r} - \mathbf{r'}| - R_C)}{|\mathbf{r} - \mathbf{r'}|}, \tag{35}$$

where Θ is the Heaviside step function, and R_C is the range of the Coulomb interactions, i.e., the radial cutoff. The Coulomb interaction matrix to be used in (32) is then

$$V^{C}_{\mathbf{G}\mathbf{G}'} = \frac{1}{\Omega}\int_{\Omega} d\mathbf{r}\int_{\Omega} d\mathbf{r}' e^{-i\mathbf{G}\mathbf{r}} V_C(\mathbf{r},\mathbf{r}') e^{i\mathbf{G}'\mathbf{r}'} = \frac{4\pi}{|\mathbf{G}|^2}[1-\cos|\mathbf{G}|R_C]\delta_{\mathbf{G}\mathbf{G}'}. \tag{36}$$

The Bethe–Salpeter kernel is

$$\Xi^{m\leftarrow m'}_{n\to n'} = \Xi^{H,m\leftarrow m'}_{n\to n'} - \frac{1}{2}\Xi^{F,m\leftarrow m'}_{n\to n'} \tag{37}$$

where the BS–Hartree kernel is

$$\Xi^{\mathrm{H},m\leftarrow m'}_{n\to n'} = \frac{1}{\Omega_{\mathrm{sc}}}\sum_{\mathbf{G}_1\mathbf{G}_2}\rho^{*}_{nm}(\mathbf{G}_1)\, V^{C}_{\mathbf{G}_1\mathbf{G}_2}\rho_{n'm'}(\mathbf{G}_2), \tag{38}$$

and the BS–Fock kernel is

$$\Xi^{\mathrm{F},m\leftarrow m'}_{n\to n'} = \frac{1}{\Omega_{\mathrm{sc}}}\sum_{\mathbf{G}_1\mathbf{G}_2}\rho^{*}_{nn'}(\mathbf{G}_1) W^{0}_{\mathbf{G}_1\mathbf{G}_2}(\omega=0)\rho_{mm'}(\mathbf{G}_2). \tag{39}$$

Here, the index '0' in W, S, Γ, and Σ^{C} emphasizes that we consider the screened interaction in a self-standing molecule. Finally, considering that the interaction V_C prevents the correlations between the conductivities in the adjacent cells, the conductivity of an isolated molecule is equal to the conductivity per unit cell

$$\sigma_{\mu\nu}(\omega) = \int_{\Omega_{\mathrm{sc}}} d\mathbf{r}\int_{\Omega_{\mathrm{sc}}} d\mathbf{r}'\sigma^{3D}_{\mu\nu}(\mathbf{r},\mathbf{r}',\omega). \tag{40}$$

After using (19) in (40), the optical conductivity of a single molecule becomes

$$\sigma_{\mu\nu}(\omega) = \Omega_{\mathrm{sc}}\sigma^{\mu\nu,3D}_{\mathbf{G}=0\mathbf{G}'=0}(\omega). \tag{41}$$

After combining Equations (9), (20), and (41), we determine the explicit expression for the surface optical conductivity

$$\tilde{\sigma}_{\mu\nu}(\omega) = \frac{2i}{\omega S_{\mathrm{fcc}}}\sum_{nm}\sum_{n'm'} j^{\mu}_{nm}(\mathbf{G}=0)\mathcal{K}^{m\leftarrow m'}_{n\to n'}(\omega)[j^{\nu}_{n'm'}(\mathbf{G}'=0)]^{*}, \tag{42}$$

which can be used in Dyson's equation for the electric field propagator (10). It is important to note that the dimension of the conductivity (42) is exactly the quantum of conductance $G_0 = \frac{2\pi e^2}{h}$, already the standardized unit for describing the optical conductivity in 2D crystals [28,47,65]. Accordingly, the $\tilde{\sigma}_{\mu\nu}(\omega)$ represents the optical conductivity of one (e.g., i-th) molecular layer.

2.3. Optical Conductivity in a Molecule Physisorbed at a Dielectric Surface

We assume that a fullerene molecule, centered at $z = z_i$, is physisorbed at the supporting crystal occupying the $z < 0$ half-space, as illustrated in Figure 3.

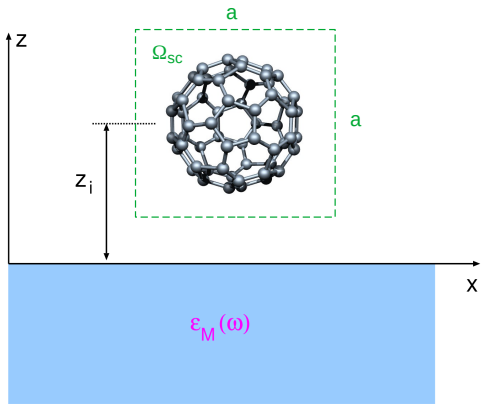

Figure 3. The fullerene molecule C_{60} centered at $z = z_i$ is physisorbed at the supporting crystal occupying the half-space $z < 0$, with the dielectric properties approximated by the macroscopic dielectric function $\epsilon_M(\omega)$.

We further assume that the bonding between the molecule and the supporting crystal has the vdW character, which implies a small electronic overlap between the molecule and the substrate and, therefore, a small impact on the short-range electronic correlations to the molecular QP and optical properties. More precisely, the processes involving the electronic hopping between the molecule and the supporting crystal are neglected. However, we shall retain the processes of scattering an electron or a hole or an excited electron–hole pair by the potential induced at the crystal surface, ΔV.

If we have two valence electrons at points $\mathbf{r}$ and $\mathbf{r}'$ in a self-standing molecule, they interact via the bare Coulomb truncated potential V_C (35), but they also polarize the molecule itself so that the total interaction between them is given by the potential W^0, obtained as the solution of Equation (32). After the polarizable surface is brought close to the molecule, the electrons at $\mathbf{r}$ and $\mathbf{r}'$ polarize the surface as well so that the interaction between them, neglecting the polarization of the molecule, becomes

$$V_S(\mathbf{r}, \mathbf{r}', \omega) \; = \; V_C(\mathbf{r}, \mathbf{r}') + \Delta V_S(\mathbf{r}, \mathbf{r}', \omega), \tag{43}$$

where $\Delta V_S(\mathbf{r}, \mathbf{r}', \omega)$ is the induced dynamic Coulomb potential coming from the excitations of the electronic modes or phonons at the surface. The total interaction between the electrons (including the polarization of the molecule) is then the solution of Dyson's equation

$$W^S_{\mathbf{G}\mathbf{G}'}(\omega) = V^S_{\mathbf{G}\mathbf{G}'}(\omega) + \sum_{\mathbf{G}_1\mathbf{G}_2} V^S_{\mathbf{G}\mathbf{G}_1}(\omega)\chi^0_{\mathbf{G}_1\mathbf{G}_2}(\omega)W^S_{\mathbf{G}_2\mathbf{G}'}(\omega), \tag{44}$$

where

$$\Delta V^S_{\mathbf{G}\mathbf{G}'}(\omega) = \frac{1}{\Omega_{sc}} \int_{\Omega_{sc}} d\mathbf{r} \int_{\Omega_{sc}} d\mathbf{r}' e^{-i\mathbf{G}\mathbf{r}} \Delta V_S(\mathbf{r}, \mathbf{r}', \omega) e^{i\mathbf{G}'\mathbf{r}'}. \tag{45}$$

Here, the integration is constrained within the unit cell Ω_{sc} centered at $\mathbf{r}_0 = (0, 0, z_i)$ (to avoid interaction with the neighboring molecules, via ΔV_S), as shown in Figure 3. The induced interaction in the region $z > 0$ can be written as [62]

$$\Delta V(\mathbf{r}, \mathbf{r}', \omega) = \int \frac{d\mathbf{Q}}{(2\pi)^2} v_Q D(\mathbf{Q}, \omega) e^{i\mathbf{Q}(\boldsymbol{\rho}-\boldsymbol{\rho}')} e^{-Q(z+z')}, \tag{46}$$

where $v_Q = \frac{2\pi}{|\mathbf{Q}|}$. Since the supporting crystal dielectric response is approximated by the local 3D macroscopic dielectric function $\epsilon_M(\omega)$, the surface excitation propagator can be approximated as [68]

$$D(\mathbf{Q}, \omega) \approx D(\omega) = \frac{1 - \epsilon_M(\omega)}{1 + \epsilon_M(\omega)}. \tag{47}$$

After (46) and (47) are used in (45), we have

$$\Delta V^{\mathrm{S}}_{\mathbf{G}\mathbf{G}'}(\omega) = \frac{D(\omega)}{\Omega_{\mathrm{sc}}} \int \frac{d\mathbf{Q}}{(2\pi)^2} v_Q e^{-2Qz_i} F_{\mathbf{G}}(\mathbf{Q}) F^*_{\mathbf{G}'}(\mathbf{Q}), \tag{48}$$

where the form factors are defined as

$$F_{\mathbf{G}}(\mathbf{Q}) = 8(-1)^{n_z} \frac{\sin[(Q_x - G_x)\frac{a}{2}] \sin[(Q_y - G_y)\frac{a}{2}] \sinh[Q\frac{a}{2}]}{(Q_x - G_x)(Q_y - G_y)(Q + iG_z)}.$$

The reciprocal vectors of the sc lattice are $\mathbf{G} = (G_x, G_y, G_z)$, where $G_x = \frac{2\pi n_x}{a}$, $G_y = \frac{2\pi n_y}{a}$, $G_z = \frac{2\pi n_z}{a}$ and $n_x, n_y, n_z \in \mathbb{Z}$. After we determine the 'bare' potential (which includes the polarization of the surface) V_{S} and the 'total' potential (which includes the polarization of the surface and of the molecule) W_{S}, the calculation of the QP and optical properties of a molecule near the dielectric surface is equal to the procedure described in Section 2.2, except for that in the BS–Hartree kernel (38), we need to replace

$$V^{\mathrm{C}}_{\mathbf{G}_1\mathbf{G}_2} \to V^{\mathrm{S}}_{\mathbf{G}_1\mathbf{G}_2}(\omega),$$

in the BS–Fock kernel (39)

$$W^0_{\mathbf{G}_1\mathbf{G}_2}(\omega = 0) \to W^{\mathrm{S}}_{\mathbf{G}_1\mathbf{G}_2}(\omega = 0),$$

and the spectrum of the electronic excitations (28) used to calculate the correlation self-energy (26) is

$$S^0_{\mathbf{G}\mathbf{G}'}(\omega) \to S^{\mathrm{S}}_{\mathbf{G}\mathbf{G}'}(\omega) = -\frac{1}{\pi} Im W^{\mathrm{S}}_{\mathbf{G}\mathbf{G}'}(\omega). \tag{49}$$

2.4. Computational Details

The fullerene KS orbitals $\phi_n(\mathbf{r})$ and energies E_n were calculated using the plane-wave self-consistent field DFT code (PWSCF) within the QUANTUM ESPRESSO (QE) package [69]. The core-electron interaction was approximated by the norm-conserving pseudopotentials [70,71] so that the number of occupied valance states was 120. The exchange-correlation (XC) potential was approximated by the Perdew–Burke–Ernzerhof (PBE) generalized gradient approximation (GGA) functional [72]. The plane-wave cut-off energy was 60 Ry. The molecules were arranged in the simple cubic Bravais lattice of the unit cell $a = 18$ Å with one molecule per unit cell. Since there was no intermolecular overlap, the ground state electronic density was calculated at the Γ point only. The geometries were fully relaxed, with all forces $\lesssim$0.02 eV/Å. The RPA 'time-ordered' screened Coulomb interactions $W^{0,\mathrm{S}}$ (Equations (32) and (44)) were calculated using the energy cut-off 2 Ry (∼27 eV), and the band summations '(n, m)' in the irreducible polarizability (33) were performed over 240 molecular states. The exchange self-energy (25) was calculated using the energy cut-off 8 Ry (∼109 eV) and the correlation self-energy (26) was determined (according to the cut-off in W_0) using the energy cut-off 2 Ry (∼27 eV); the band summation 'm' was performed using 240 molecular orbitals. The BS–Hartree kernel (38) and the 'bare' BS–Fock kernel (the Equation (39), derived using the bare interaction V_{C}), were calculated using the energy cut-off 8 Ry (∼109 eV); the induced Fock kernel (the Equation (39), derived using the induced interaction $W_{0,\mathrm{S}} - V_{\mathrm{C}}$), was calculated using the energy cut-off 2 Ry (∼27 eV). During the evaluation of the BSE–HF kernels, we used 42 occupied (HOMO − 41, ..., HOMO) and 42 unoccupied (LUMO, ..., LUMO + 41) molecular states, i.e., the dimensions of the BSE–HF kernel matrix was $2 \times 42 \times 42 = 3528$. To achieve the accurate (experimental) exciton energy, the calculation was performed beyond the Tamm–Dancoff approximation. The damping parameters δ used in (31) and in (33) were 50 meV and 200 meV, respectively. We

assume that the dielectric medium was vacuum (i.e., $\epsilon_0 = 1$), and that the substrate was the aluminum-oxide Al_2O_3, described by the macroscopic dielectric function

$$\epsilon_{\mathrm{M}}(\omega) = 1/\epsilon^{-1}_{\mathbf{G}=0\mathbf{G}'=0}(\mathbf{q} \approx 0, \omega), \tag{50}$$

where the dielectric matrix is $\hat{\epsilon} = \hat{\mathrm{I}} - \hat{V}\hat{\chi}^0$. The irreducible polarizability χ^0 is determined using Equation (33) for $\Omega_{\mathrm{sc}} \to \Omega$, $n \to (n, \mathbf{k})$ and $m \to (m, \mathbf{k} + \mathbf{q})$. Here $\mathbf{k}$, $\mathbf{q}$, and $\mathbf{G}$ are the 3D wave vector, the transfer wave vector, and the reciprocal lattice vector, respectively, corresponding to the bulk Al_2O_3 crystal. The bare Coulomb interaction is $V_{\mathbf{GG}'}(\mathbf{q}) = \frac{4\pi}{|\mathbf{q}+\mathbf{G}|^2}\,\delta_{\mathbf{GG}'}$. The ground state electronic density of the bulk Al_2O_3 is calculated using $9 \times 9 \times 3$ K-mesh, the plane-wave cut-off energy is 50 Ry, and the Bravais lattices are hexagonal (12 Al and 18 O atoms in the unit cell) with the lattice constants $a_{\mathrm{Al_2O_3}} = 4.76$ Å and $c_{\mathrm{Al_2O_3}} = 12.99$ Å. The Al_2O_3 irreducible polarizability χ^0 is calculated using the $21 \times 21 \times 7$ k-point mesh and the band summations (n, m) are performed over 120 bands. The damping parameter is $\delta = 100$ meV and the temperature is $T = 10$ meV. For the optically small wave vectors $\mathbf{q} \approx 0$, the crystal local field effects are negligible, i.e., the crystal local field effects cut-off energy is set to zero. Using this approach, the $\mathrm{Re}\epsilon_{\mathrm{M}}$ is almost constant ($\mathrm{Re}\epsilon_{\mathrm{M}} \approx 3$) for low frequencies ($\omega < 3$ eV), i.e., in the IR and visible range, while $\mathrm{Im}\epsilon_{\mathrm{M}}$ is equal to zero up to the band gap energy (E_g~6 eV). Therefore, Al_2O_3 is a good choice for the substrate in the visible and near-UV frequency range, since its electronic excitations are above that range, and its IR active SO phonons (at $\omega_{\mathrm{SO}} < 100$ meV) [73] are far below the C_{60} excitons, which means that in the frequency range of interest, there is no dissipation of the electromagnetic energy in the substrate (it is transparent). In addition to that, the dielectric function is mostly constant, but in this calculation, we used the fully dynamical and complex $\epsilon_{\mathrm{M}}(\omega)$. The integration in (48) was performed over the two-dimensional wave vectors $\mathbf{Q} = (Q_x, Q_x)$ using a 121×121 rectangular mesh and the cut-off wave vector $Q_{\mathrm{C}} = 0.5$ a.u. For the radial cut-off in the truncated interaction (36), we used $R_{\mathrm{C}} = a/2 = 9$ Å.

3. Results and Discussion

Strong exciton–photon hybridization usually occurs due to the large overlap between excitons of large oscillatory strengths and confined photons. This is experimentally achieved by placing nanostructures or molecules of large oscillatory strength in a metallic cavity. Our goal here was to explore the electromagnetic eigenmodes, which are a mixture of 'free' s(TE) photons and excitons, i.e., a 'free' traveling photon (not confined between metallic walls) captured by an exciton and 'trapped' in a molecular nanostructure. This concept makes it possible to clearly estimate the contribution of the 'free' photon in the hybrid exciton–photon mode.

First, we determined the QP and optical properties of a self-standing layer of the C_{60} molecules, which corresponded with the properties of the gas-phase molecule, since at the G_0W_0-BSE stage of the calculations, the molecules were not coupled. The calculated G_0W_0 HOMO-LUMO gap was $E_g = 4.66$ eV, which is in good agreement with the experimental value 5 eV [74–77]. When a molecular layer is deposited on an Al_2O_3 dielectric surface, the band gap reduces to $E_g = 4.26$ eV. Here, the separation was chosen to be $z_0 = 6.5$ Å which corresponds to the characteristic vdW atom–atom separation of 3 Å (Note that z_0 is defined as the distance between the substrate and the center of the molecule, as denoted in Figure 1, so the C_{60} molecule radius (3.57 Å) has to be added to the vdW atom–atom distance). For comparison, we determined the HOMO-LUMO gap for the molecule at a silver (Ag) surface also described in terms of the *ab initio* macroscopic dielectric function. For the same separation ($z_0 = 6.5$ Å), the gap was $E_g = 3.81$ eV; compared with the insulator surface, the reduction is twice as strong. The image theory estimation of the HOMO-LUMO gap at the metallic surface is E_g~3.56 eV which, as expected, overestimates the G_0W_0 result. Figure 4a shows the calculated G_0W_0-BSE optical conductivities $\tilde{\sigma}_x(\omega)$ in the self-standing molecular layer (black solid) and in the molecular layer deposited at the Al_2O_3

dielectric surface (cyan dashed). For comparison, the experimental optical absorption in the fullerene C_{60} [78] is presented by the red circles. This experimental study, as well as some others [79,80], show three broad excitation bands at $\omega_{ex1}\sim$ 3.9 eV, $\omega_{ex2}\sim$4.9 eV and $\omega_{ex3}\sim$6 eV, which is in very good agreement with our results. It should be emphasized that, since the band gap is $E_g = 4.66$ eV, only the excitation band ω_{ex1} can be considered as an exciton by definition, and its binding energy is $E_g - \hbar\omega_{ex1}\sim$0.76 eV. In the literature, the strong maximum ω_{ex3} is usually referred to as the π plasmon [81,82]. All three excitons are the result of the electronic transitions within the C_{60} π-complex [83]. When the molecule is deposited at the Al_2O_3 surface, the excitation band barely changes at all, due to the well-known cancellation effect: the substrate weakens the interaction between the excited electron and the hole, which reduces the exciton binding energy and, therefore, cancels the gap reduction. This phenomenon was studied in detail in references [62,66,84]. Since the influence of the dielectric surface on the molecular optical conductivity is weak, we shall further approximate $\tilde{\sigma}^x_i(\omega) \approx \tilde{\sigma}^x(\omega)$, where $\tilde{\sigma}^x(\omega)$ is the optical conductivity in the self-standing molecular single layer, i.e., for $z_0 \to \infty$.

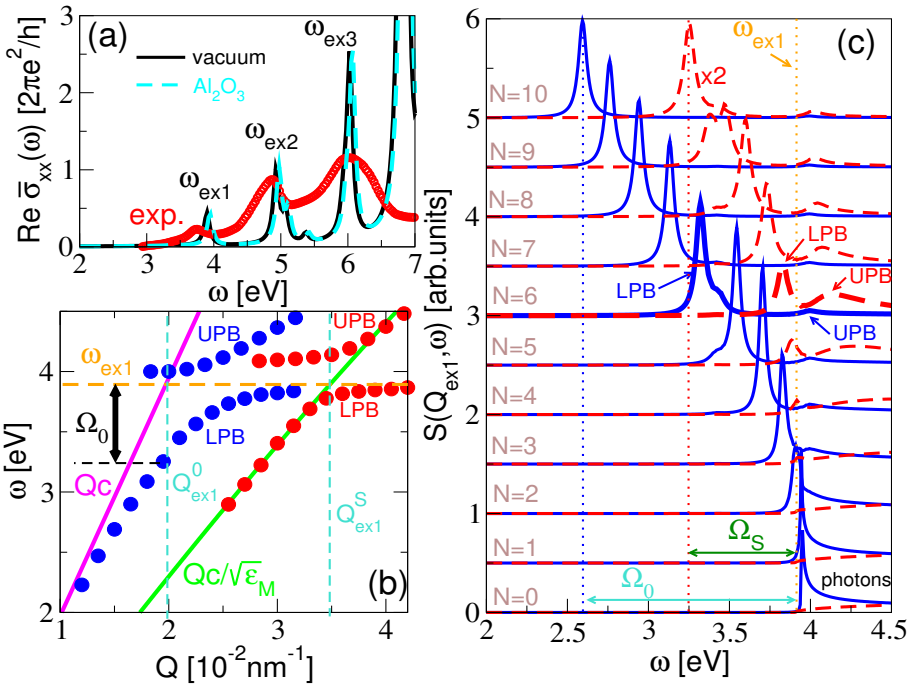

Figure 4. (**a**) The optical conductivities $\tilde{\sigma}_{xx}(\omega)$ in the C_{60} single layer in vacuum (black solid), in the C_{60} single layer at the Al_2O_3 dielectric surface (cyan dashed) (where $z_0 = 6.5$ Å), and the experimental optical absorption in the gas phase fullerene C_{60} (red circles). (**b**) The lower and upper exciton–polariton branches, LPB and UPB, respectively, in the self-standing C_{60} film (blue dots) and the C_{60} film deposited at the Al_2O_3 surface (red dots). The LPB corresponds to the dispersion relation of the exciton–polariton $\omega_{\text{ex1-pol}}(Q)$ appearing in Equation (53). The number of C_{60} layers is $N = 6$. (**c**) The spectra of the s(TE)-polarized electromagnetic modes $S(Q_{ex1},\omega)$ in the self-standing C_{60} films for $Q^0_{\text{ex1}} = 0.02\,\text{nm}^{-1}$ (blue solid) and in the C_{60} films at the Al_2O_3 surface for $Q_{\text{ex1}} = 0.035\,\text{nm}^{-1}$ (red dashed). The number of the single layers is $N = 0, 1, 2, 3, \ldots, 10$, where the case $N = 0$ corresponds to the spectrum of the free photons in vacuum or at the vacuum/Al_2O_3 interface (the photon continuum). All spectra for the supported films are multiplied by factor 2.

This means that the impact of the dielectric substrate on the electromagnetic modes in the C_{60} films is reduced to the propagator Γ^{sc}, which appears in Dyson's Equation (14). The spectra of the s(TE)-polarized electromagnetic modes in the C_{60} films will be analyzed using the real part of the propagator $\mathcal{E}$ in the topmost molecular layer

$$S(Q,\omega) \;=\; Re\mathcal{E}_{xx}(|\mathbf{Q}|\mathbf{y},\omega,z_{\text{N}},z_{\text{N}}). \tag{51}$$

As already mentioned, the spacing parameters were chosen to be $z_0 = 6.5$ Å and $\Delta = 8.1$ Å. In the near field spectroscopy experiment, the incident photon of the wavelength

$$\lambda_{\text{ex1}} = \frac{2\pi c}{\omega_{\text{ex1}}\sqrt{\epsilon(\omega_{\text{ex1}})}} \tag{52}$$

couples to polarization modes in some sub-wavelength nanostructure (e.g., AFM tip) and is scattered (diffracted) to all $\lambda > \lambda_{\text{ex1}}$ and $\lambda < \lambda_{\text{ex1}}$ so that it could excite all radiative electromagnetic modes, as well as all evanescent ones at a fixed frequency ω_{ex1}. The Rabi splitting (the measure of the free-photon participation in the exciton–polariton mode) is defined as the difference between the exciton ω_{ex1} and the exciton–polariton $\omega_{\text{ex1-pol}}$

$$\hbar\Omega = \hbar\omega_{\text{ex1}} - \hbar\omega_{\text{ex1-pol}}(Q_{ex1}), \tag{53}$$

where $Q_{ex1} = 2\pi/\lambda_{\text{ex1}}$ is the wave vector at which the exciton ω_{ex1} and the photon cross.

Figure 4b shows the dispersion relations of the exciton–polaritons $\omega_{\text{ex1-pol}}(Q)$ in the self-standing C_{60} film (blue dots), and in the C_{60} film deposited at a Al_2O_3 surface (red dots). The number of C_{60} single layers in the film was chosen to be $N = 6$. The energies of the exciton–polaritons $\omega_{\text{ex1-pol}}(Q)$ correspond to the maxima in the spectral function $S(Q,\omega)$, appearing below the exciton energy ω_{ex1} [see Figure 4c]. For the self-standing film, $\epsilon(\omega) = 1$, so that the crossing wave vector, according to the Equation (52), was $Q^0_{\text{ex1}} = 0.02$ nm^{-1}, and the Rabi splitting, according to the Equation (53), was $\hbar\Omega_0 = 650$ meV. The red dots in Figure 4b show that the presence of the substrate reduces the bending of the exciton–polariton dispersion relation significantly, therefore reducing the corresponding Rabi splitting. In this case, $\epsilon(\omega) = \epsilon_{\text{M}}(\omega)$, which gives the crossing wave vector $Q^{\text{S}}_{\text{ex1}} = 0.035$ nm^{-1} and, thus, the Rabi splitting $\hbar\Omega_{\text{S}} = 103$ meV.

Figure 4c shows the spectra of the s(TE)-polarized electromagnetic modes $S(Q_{ex1},\omega)$ in the self-standing C_{60} films for $Q^0_{\text{ex1}} = 0.02$ nm^{-1} (blue solid) and in the C_{60} films deposited at the Al_2O_3 surface for $Q^S_{\text{ex1}} = 0.035$ nm^{-1} (red dashed). The number of layers is set to be $N = 0, 1, 2, 3, \ldots, 10$, where the case $N = 0$ corresponds to the spectra of the free photons in vacuum or at the vacuum/Al_2O_3 interface (photons continuum). Due to the lower intensity, all spectra for the supported films were multiplied by factor 2. We can clearly see the exciton–polariton peaks separating from the photon continuum as the number of layers increases. In the self-standing films, the exciton–polariton is already well separated for $N = 2$, while in the supported films, it occurs for $N = 4$. For $N = 10$, the giant light–matter coupling was achieved providing large Rabi splitting $\Omega_0 = 1334$ meV and $\Omega_S = 670$ meV in the self-standing and the supported films, respectively. Here we limited our study to the exciton–polaritons in the quasi-2D nanostructures so that the maximum number of the molecular layers was limited to $N = 10$, still satisfying the sub-wavelength limit $\lambda_{\text{ex1}} > (N-1)\Delta$. For a further increase of the number of layers N, the Rabi splitting continued to increase, but the experimental limitations in the realization of such a system raise the question of the plausibility of such a result.

We need to emphasize that the anti-crossing behavior and the Rabi splitting into the lower polariton band (LPB) and the upper polariton band (UPB) is a well-defined concept only when describing the interaction between the well-defined eigenmodes, such as excitons and cavity photons [33] or BSWs [48]. In our case, the only well-defined modes (boson) were the excitons ω_{ex1}-ω_{ex3}. On the other hand, the photons appeared as a continuum of eigenmodes above the light lines Qc or $Qc/\sqrt{\epsilon_{\text{M}}}$. This means that it only made sense to observe the deformation of the exciton dispersion ω_{ex1}, characterized by the exciton bending parameter Ω. However, in Figure 5, it seems that the edge of the photon continuum Qc or $Qc/\sqrt{\epsilon_{\text{M}}}$ behaves similar to a well-defined eigenmode, so in Figure 4b,c we also introduced and denoted the LPB and UPB, exactly as they appear in Figure 5b,e. The LPB corresponds to the exciton–polariton dispersion relation $\omega_{\text{ex1-pol}}(Q)$ appearing in (53).

To present a more extensive picture of the electromagnetic modes in the C_{60} films, including the hybridizations of the photon and the higher excitons ω_{ex2} and ω_{ex3}, Figure 5a–c show the spectral intensity of the s(TE)-polarized electromagnetic modes $S(Q,\omega)$ in the self-standing C_{60} films for $N = 3$, 6, and 9, respectively. Figure 5d–f show the same for the C_{60} films deposited at the Al_2O_3 surface. It is immediately obvious that the most intensive electromagnetic modes occur in the evanescent regions $\omega < Qc$ and $\omega < Qc/\epsilon_M(\omega)$, for the self-standing and supported films, respectively. These modes produce an electric field, which spreads within the film and exponentially decays outside of the film [as illustrated in Figure 2b], which is one of the inherent properties of the 2D exciton–polaritons. Moreover, as the field is more confined, it is stronger, so that the polariton modes confined at a sub-wavelength scale are very interesting for many applications. The free photon continua can be seen as the low-intensity patterns in the regions $\omega > Qc$, and $\omega > Qc/\epsilon_M(\omega)$ in the self-standing and supported films, respectively, with their intensity weakening with the number of layers N. If the electromagnetic eigenmode, for example in the C_{60} film at the Al_2O_3, would occur in the region $\omega > Qc/\epsilon_M(\omega)$, it would be irradiated (decay radiatively) into the Al_2O_3 crystal, so that these modes appear only as weak resonances. Such weak resonances can be seen as weak horizontal patterns (parallel with the excitons ω_{ex1}-ω_{ex3}) entering the radiative region.

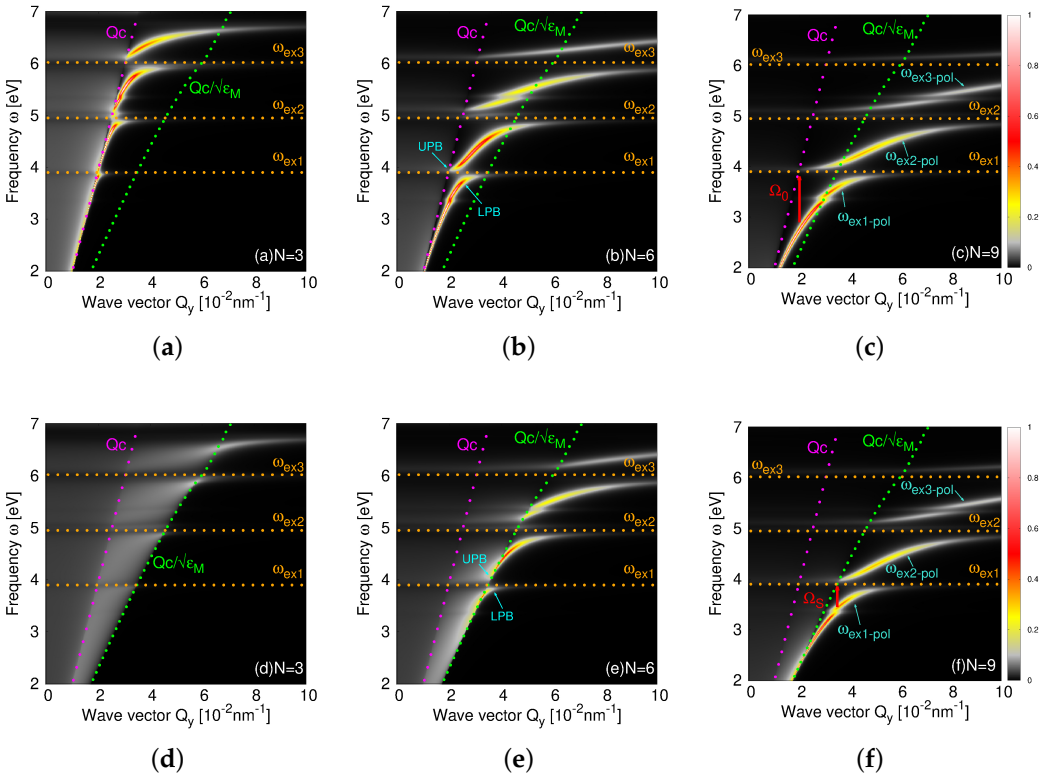

Figure 5. The spectral intensity of the s(TE)-polarized electromagnetic modes $S(Q,\omega)$ in the self-standing C_{60} films for (**a**) $N = 3$, (**b**) $N = 6$, and (**c**) $N = 9$. Figures (**d**–**f**) show the same for the C_{60} films deposited at the Al_2O_3 surface. In both cases, the strong electromagnetic modes ($\omega_{ex1\text{-}pol}$, $\omega_{ex2\text{-}pol}$, and $\omega_{ex3\text{-}pol}$) occur in the evanescent regions $\omega < Qc$ and $\omega < Qc/\epsilon_M(\omega)$.

In Figure 5a, we can see the beginning of the hybridization between the free photon and the three C_{60} excitons (ω_{ex1}-ω_{ex3}), which visibly intersect the photon line $\omega = Qc$. In Figure 5b,c, the photon line is already significantly deformed between the excitons and pushed far into the evanescent region, which means that the photon Qc and the three excitons ω_{ex1}, ω_{ex2}, and ω_{ex3} are strongly coupled and converted into three exciton–polaritons $\omega_{ex1\text{-}pol}$, $\omega_{ex2\text{-}pol}$, and $\omega_{ex3\text{-}pol}$. In Figure 5d–f, the exciton–polaritons are less

intense and pushed into the evanescent region $\omega < Qc/\epsilon_{\mathrm{M}}(\omega)$, the use of the substrate obviously weakens the intensity of the exciton–polaritons. However, in Figure 5e,f, we can see the formation of the three strong exciton–polariton modes $\omega_{\text{ex1-pol}}$–$\omega_{\text{ex3-pol}}$, for larger numbers of layers $N = 6$ and 9, respectively. Finally, this confirms that the strong binding between the transverse s(TE) photon and the molecular excitons is a realistic physical phenomenon that can be achieved experimentally. The use of a metal substrate is not recommended because a metallic surface will strongly quench the exciton–polariton modes. To support this argument, we performed the same calculation using a silver (Ag) substrate and obtained much weaker exciton–polariton modes.

Finally, we noticed that the hybridization between the exciton and the photon increases weakly if just the exciton oscillatory strength (e.g., S) increases, but strongly if the number of spatially separated molecular layers N increases. For example, the exciton–photon binding is much stronger in the N-separated layers of the oscillatory strength S than in one layer of the oscillatory strength N× S. This suggests that the photon-exciton coupling can be increased simply by increasing the number of layers N in a multilayered van der Waals heterostructure.

4. Conclusions

We showed that the 2D-layered heterostructures, consisting of a larger number of exciton-active single layers or 2D crystals (e.g., $N > 5$), can support evanescent s(TE)-polarized exciton–polaritons with strong photonic character. We obtained giant Rabi splitting of more than $\Omega_0 = 1000$ meV and $\Omega_S = 500$ meV in the self-standing and supported C_{60} films for $N = 10$, respectively. This investigation has fundamental and practical contributions. We predict the existence of the evanescent s(TE) polarization modes with significant photonic character, which vanish exactly without the photon admixture (for $c \to \infty$). Unlike the well-known p(TM) polarization modes (e.g., the plasmon polariton for $c \to \infty$ collapses into a plasmon), this is a new fundamental contribution. We also demonstrated that exciton–photon coupling can be manipulated simply by changing the number of single layers (N) in a vdW-layered heterostructure. Moreover, due to the fact that the vdW heterostructure with a thickness of just a few molecular (or atomic) layers supports the confined photons, it can be easily implemented in the photonic integrated circuits or photonics chips. The disadvantage of these types of photonic modes is that they do not couple directly to the free photons (external light). However, once excited, these modes can be easily manipulated (since they are trapped in the nanostructure). For example, by patterning the vdW nanoribbons on a dielectric wafer (patterning the photonics circuits), the direction of the photon propagation can easily be modified. Moreover, the exciton–polaritons can be easily switched (at the contact) into evanescent modes in another nanostructure. Finally, these layered vdW heterostructures can be applied in photonic devices, such as light sources (LED), telecommunications (as waveguides or optical cables), or chemical and biological sensing.

Author Contributions: Conceptualization, V.D.; methodology, V.D.; software, V.D. and L.M.; validation, V.D. and L.M.; formal analysis, V.D.; investigation, V.D. and L.M.; resources, V.D. and L.M.; data curation, V.D.; writing—original draft preparation, V.D.; writing—review and editing, V.D. and L.M.; visualization, V.D.; supervision, V.D.; project administration, V.D.; funding acquisition, V.D. All authors have read and agreed to the published version of the manuscript.

Funding: This research was funded by the Croatian Science Foundation (grant no. IP-2020-02-5556) and the European Regional Development Fund for the "QuantiXLie Centre of Excellence" (grant KK.01.1.1.01.0004).

Institutional Review Board Statement: Not applicable.

Informed Consent Statement: Not applicable.

Data Availability Statement: Not applicable.

Acknowledgments: The authors acknowledge support from the Donostia International Physic Center (DIPC) computing center, which provided the computational resources.

Conflicts of Interest: The authors declare no conflict of interest.

References

1. Basov, D.N.; Asenjo-Garcia, A.; Schuck, P.J.; Xiaoyang, Z.; Rubio, A. Polariton panorama. *Nanophotonics* **2021**, *10*, 549–577. [CrossRef]
2. Deng, H.; Haug, H.; Yamamoto, Y. Exciton-polariton Bose-Einstein condensation. *Rev. Mod. Phys.* **2010**, *82*, 1489. [CrossRef]
3. Weisbuch, C.; Nishioka, M.; Ishikawa, A.; Arakawa, Y. Observation of the coupled exciton-photon mode splitting in a semiconductor quantum microcavity. *Phys. Rev. Lett.* **1992**, *69*, 3314. [CrossRef]
4. Ribeiro, R.F.; Martínez-Martínez, L.A.; Du, M.; Campos-Gonzalez-Angulo, J.; Yuen-Zhou, J. Polariton chemistry: Controlling molecular dynamics with optical cavities. *Chem. Sci.* **2021**, *9*, 6325–6329. [CrossRef]
5. Kasprzak, J.; Richard, M.; Kundermann, S.; Baas, A.; Jeambrun, P.; Keeling, J.M.J.; Marchetti, F.M.; Szymańska, M.H.; André, R.; Staehli, J.L.; et al. Bose–Einstein condensation of exciton polaritons. *Nature* **2006**, *443*, 409–414. [CrossRef] [PubMed]
6. Balili, R.; Hartwell, V.; Snoke, D.; Pfeiffer, L.; West, K. Bose-Einstein Condensation of Microcavity Polaritons in a Trap. *Science* **2007**, *316*, 1007–1010. [CrossRef]
7. Christopoulos, S.; Von Högersthal, G.B.H.; Grundy, A.J.D.; Lagoudakis, P.G.; Ka-vokin, A.V.; Baumberg, J.J.; Christmann, G.; Butté, R.; Feltin, E.; Carlin, J.F.; et al. Room-Temperature Polariton Lasing in Semiconductor Microcavities. *Phys. Rev. Lett.* **2007**, *98*, 126405. [CrossRef]
8. Baumberg, J.J.; Kavokin, A.V.; Christopoulos, S.; Grundy, A.J.D.; Butté, R.; Christ-mann, G.; Solnyshkov, D.D.; Malpuech, G.; von Högersthal, G.B.H.; Feltin, E.; et al. Spontaneous Polarization Buildup in a Room-Temperature Polariton Laser. *Phys. Rev. Lett.* **2008**, *101*, 136409. [CrossRef]
9. Zhang, S.; Chen, J.; Shi, J.; Fu, L.; Du, W.; Sui, X.; Mi, Y.; Jia, Z.; Liu, F.; Shi, J.; et al. Trapped Exciton–Polariton Condensate by Spatial Confinement in a Perovskite Microcavity. *ACS Photonics* **2020**, *7*, 327–337. [CrossRef]
10. Bao, W.; Liu, X.; Xue, F.; Zheng, F.; Tao, R.; Wang, S.; Xia, Y.; Zhao, M.; Kim, J.; Yang, S.; et al. Observation of Rydberg exciton polaritons and their condensate in a perovskite cavity. *Proc. Natl. Acad. Sci. USA* **2019**, *116*, 20274–20279. [CrossRef]
11. Horikiri, T.; Byrnes, T.; Kusudo, K.; Ishida, N.; Matsuo, Y.; Shikano, Y.; Löffler, A.; Höfling, S.; Forchel, A.; Yamamoto, Y. Highly excited exciton-polariton condensates. *Phys. Rev. B* **2017**, *95*, 245122. [CrossRef]
12. Ramasubramaniam, A. Large excitonic effects in monolayers of molybdenum and tungsten dichalcogenides. *Phys. Rev. B* **2012**, *86*, 115409. [CrossRef]
13. Li, Y.; Chernikov, A.; Zhang, X.; Rigosi, A.; Hill, H.M.; van der Zande, A.M.; Chenet, D.A.; Shih, E.M.; Hone, J.; Heinz, T.F. Measurement of the optical dielectric function of monolayer transition-metal dichalcogenides: MoS_2, $MoSe_2$, WS_2, and Wse_2. *Phys. Rev. B* **2014**, *90*, 205422. [CrossRef]
14. Qiu, D.Y.; Jornada, F.H.; Louie, S.G. Optical Spectrum of MoS_2: Many-Body Effects and Diversity of Exciton States. *Phys. Rev. Lett.* **2013**, *111*, 216805. [CrossRef] [PubMed]
15. Lin, Y.; Ling, X.; Yu, L.; Huang, S.; Hsu, A.L.; Lee, Y.H.; Kong, J.; Dresselhaus, M.S.; Palacios, T. Dielectric Screening of Excitons and Trions in Single-Layer MoS_2. *Nano Lett.* **2014**, *14*, 5569–5576. [CrossRef] [PubMed]
16. Yan, J.; Jacobsen, K.W.; Thygesen, K.S. Optical properties of bulk semiconductors and graphene/boron nitride: The Bethe-Salpeter equation with derivative discontinuity-corrected density functional energies. *Phys. Rev. B* **2012**, *86*, 045208. [CrossRef]
17. Ferreira, F.; Ribeiro, R.M. Improvements in the GW and Bethe-Salpeter-equation calculations on phosphorene. *Phys. Rev. B* **2017**, *96*, 115431. [CrossRef]
18. Villegas, C.E.P.; Rodin, A.S.; Carvalho, A.C.; Rocha, A.R. Two-dimensional exciton properties in monolayer semiconducting phosphorus allotropes. *Phys. Chem. Chem. Phys.* **2016**, *18*, 27829–27836. [CrossRef]
19. Wang, X.; Jones, A.M.; Seyler, K.L.; Tran, V.; Jia, Y.; Zhao, H.; Wang, H.; Yang, L.; Xu, X.; Xia, F. Highly anisotropic and robust excitons in monolayer black phosphorus. *Nat. Nanotechnol.* **2015**, *10*, 517–521. [CrossRef]
20. Low, T.; Chaves, A.; Caldwell, J.D.; Kumar, A.; Fang, N.X.; Avouris, P.; Heinz, T.F.; Guinea, F.; Martin-Moreno, L.; Koppens, F. Polaritons in layered two-dimensional materials. *Nat. Mater.* **2017**, *16*, 182–194. [CrossRef]
21. Liu, X.; Galfsky, T.; Sun, Z.; Xia, F.; Lin, E.C.; Lee, Y.H.; Kéna-Cohen, S.; Menon, V.M. Strong light–matter coupling in two-dimensional atomic crystals. *Nat. Photonics* **2014**, *9*, 30–34. [CrossRef]
22. Dufferwiel, S.; Schwarz, S.; Withers, F.; Trichet, A.A.P.; Li, F.; Sich, M.; Del Pozo-Zamudio, O.; Clark, C.; Nalitov, A.; Solnyshkov, D.D.; et al. Exciton–polaritons in van der Waals heterostructures embedded in tunable microcavities. *Nat. Commun.* **2015**, *6*, 8579. [CrossRef] [PubMed]
23. Flatten, L.C.; He, Z.; Coles, D.M.; Trichet, A.A.P.; Powell, A.W.; Taylor, R.A.; Warner, J.H.; Smith, J.M. Room-temperature exciton-polaritons with two-dimensional WS_2. *Sci. Rep.* **2016**, *6*, 33134. [CrossRef] [PubMed]
24. Dufferwiel, S.; Lyons, T.P.; Solnyshkov, D.D.; Trichet, A.A.P.; Catanzaro, A.; Withers, F.; Malpuech, G.; Smith, J.M.; Novoselov, K.S.; Skolnick, M.S.; et al. Valley coherent exciton-polaritons in a monolayer semiconductor. *Nat. Commun.* **2018**, *9*, 4797. [CrossRef]
25. Gu, J.; Walther, V.; Waldecker, L.; Rhodes, D.; Raja, A.; Hone, J.C.; Heinz, T.F.; Ké-na-Cohen, S.; Pohl, T.; Menon, V.M. Enhanced nonlinear interaction of polaritons via excitonic Rydberg states in monolayer Wse_2. *Nat. Commun.* **2021**, *12*, 2269. [CrossRef]

26. Förg, M.; Colombier, L.; Patel, R.K.; Lindlau, J.; Mohite, A.D.; Yamaguchi, H.; Glazov, M.M.; Hunger, D.; Högele, A. Cavity-control of interlayer excitons in van der Waals heterostructures. *Nat. Commun.* **2019**, *10*, 3697. [CrossRef]
27. Fei, Z.; Scott, M.E.; Gosztola, D.J.; Foley IV, J.; Yan, J.; Mandrus, D.G.; Wen, H.; Zhou, P.; Zhang, D.W.; Sun, Y.; et al. Nano-optical imaging of WSe_2 waveguide modes revealing light-exciton interactions. *Phys. Rev. B* **2016**, *94*, 081402(R). [CrossRef]
28. Novko, D.; Despoja, V. Cavity exciton polaritons in two-dimensional semiconductors from first principles. *Phys. Rev. Res.* **2021**, *3*, L032056. [CrossRef]
29. Lidzey, D.G.; Bradley, D.D.C.; Skolnick, M.S.; Virgili, T.; Walker, S.; Whittaker, D.M. Strong exciton-photon coupling in an organic semiconductor microcavity. *Nature* **1998**, *395*, 53–55. [CrossRef]
30. Hobson, P.A.; Barnes, W.L.; Lidzey, D.G.; Gehring, G.A.; Whittaker, D.M.; Skolnick, M.S.; Walker, S. Strong exciton–photon coupling in a low-Q all-metal mirror microcavity. *Appl. Phys. Lett.* **2002**, *81*, 3519–3521. [CrossRef]
31. Takada, N.; Kamata, T.; Bradley, D.D.C. Polariton emission from polysilane-based organic microcavities. *Appl. Phys. Lett.* **2003**, *82*, 1812–1814.
32. Kena-Cohen, S.; Forrest, S.R. Giant Davydov splitting of the lower polariton branch in a polycrystalline tetracene microcavity. *Phys. Rev. B* **2008**, *77*, 073205. [CrossRef]
33. Schwartz, T.; Hutchison, J.A.; Genet, C.; Ebbesen, T.W. Reversible Switching of Ultrastrong Light-Molecule Coupling. *Phys. Rev. Lett.* **2011**, *106*, 196405. [CrossRef] [PubMed]
34. Gambino, S.; Mazzeo, M.; Genco, A.; Di Stefano, O.; Savasta, S.; Patane, S.; Ballarini, D.; Mangione, F.; Lerario, G.; Sanvitto, D.; et al. Exploring Light-Matter Interaction Phenomena under Ultrastrong Coupling Regime. *ACS Photonics* **2014**, *1*, 1042–1048. [CrossRef]
35. Kena-Cohen, S.; Maier, S.A.; Bradley, D.D.C. Ultrastrongly Coupled Exciton–Polaritons in Metal-Clad Organic Semiconductor Microcavities. *Adv. Opt. Mater.* **2013**, *1*, 827–833. [CrossRef]
36. Martínez-Martínez, L.A.; Ribeiro, R.F.; Campos-Gonzá lez-Angulo, J.; Yuen-Zhou, J. Can Ultrastrong Coupling Change Ground-State Chemical Reactions? *ACS Photonics* **2018**, *5*, 167–176. [CrossRef]
37. Dudek, D.; Kowerdziej, R.; Pianelli, A.; Parka, J. Graphene-based tunable hyperbolic microcavity. *Sci. Rep.* **2021**, *11*, 74. [CrossRef] [PubMed]
38. Tsai, W.L.; Chen, C.Y.; Wen, Y.T.; Yang, L.; Cheng, Y.L.; Lin, H.W. Band Tunable Microcavity Perovskite Artificial Human Photoreceptors. *Adv. Mater.* **2019**, *31*, 1900231. [CrossRef]
39. Xia, K.; Sardi, F.; Sauerzapf, C.; Kornher, T.; Becker, H.W.; Kis, Z.; Kovacs, L.; Der-tli, D.; Foglszinger, J.; Kolesov, R.; et al. Tunable microcavities coupled to rare-earth quantum emitters. *Optica* **2022**, *9*, 445–450. [CrossRef]
40. Vinogradov, E.A. Vibrational polaritons in semiconductor films on metal surfaces. *Phys. Rep.* **1992**, *217*, 159–223. [CrossRef]
41. Pitarke, J.M.; Silkin, V.M.; Chulkov, E.V.; Echenique, P.M. Theory of surface plasmons and surface-plasmon polaritons. *Rep. Prog. Phys.* **2007**, *70*, 1. [CrossRef]
42. Zhang, H.; Abhiraman, B.; Zhang, Q.; Miao, J.; Jo, K.; Roccasecca, S.; Knight, M.W.; Davoyan, A.R.; Jariwala, D. Hybrid Exciton-Plasmon-Polaritons in van der Waals Semiconductor. *Nat. Commun.* **2020**, *11*, 3552. [CrossRef] [PubMed]
43. Kumar, P.; Lynch, J.; Song, B.; Ling, H.; Barrera, F.; Kisslinger, K.; Zhang, H.B.; Anantharaman, S.; Digani, J.; Zhu, H.H.; et al. Light-matter coupling in large-area van der Waals superlattices. *Nat. Nanotechnol.* **2022**, *17*, 182–189. [CrossRef] [PubMed]
44. Anantharaman, S.B.; Stevens, C.E.; Lynch, J.; Song, B.; Hou, J.; Zhang, H.; Jo, K.; Kumar, P.; Blancon, J.C.; Mohite, A.D.; et al. Self-Hybridized Polaritonic Emission from Layered Perovskites. *Nano Lett.* **2021**, *21*, 6245–6252. [CrossRef]
45. Anantharaman, S.B.; Jo, K.; Jariwala, D. Exciton–Photonics: From Fundamental Science to Applications. *ACS Nano* **2021**, *15*, 12628–12654. [CrossRef]
46. Jariwala, D.R.; Davoyan, A.; Tagliabue, G.C.; Sherrott, M.; Wong, J.A. Atwater, H. Near-Unity Absorption in van der Waals Semiconductors for Ultrathin Optoelectronics. *Nano Lett.* **2016**, *16*, 5482–5487. [CrossRef]
47. Novko, D.; Lyon, K.; Mowbray, D.J.; Despoja, V. Ab initio study of electromagnetic modes in two-dimensional semiconductors: Application to doped phosphorene. *Phys. Rev. B* **2021**, *104*, 115421. [CrossRef]
48. Pirotta, S.; Patrini, M.; Liscidini, M.; Galli, M.; Dacarro, G.; Canazza, G.; Guizzetti, G.; Comoretto, D.; Bajoni, D. Strong coupling between excitons in organic semiconductors and Bloch surface waves. *Appl. Phys. Lett.* **2014**, *104*, 051111. [CrossRef]
49. Lerario, G.; Ballarini, D.; Fieramosca, A.; Cannavale, A.; Genco, A.; Mangione, F.; Gambino, S.; Dominici, L.; De Giorgi, M.; Gigli, G.; et al. Hig-speed flow of interacting organic polaritons. *Light. Sci. Appl.* **2017**, *6*, e16212. [CrossRef]
50. Barachati, F.; Fieramosca, A.; Hafezian, S.; Gu, J.; Chakraborty, B.; Ballarini, D.; Martinu, L.; Menon, V.; Sanvitto, D.; Kena-Cohen, S. Interacting polariton fluids in a monolayer of tungsten disulfide. *Nat. Nanotechnol.* **2018**, *13*, 906–909. [CrossRef]
51. Hou, S.; Khatoniar, M.; Ding, K.; Qu, Y.; Napolov, A.; Menon, V.M.; Forrest, S.R. Ultralong-Range Energy Transport in a Disordered Organic Semiconductor at Room Temperature Via Coherent Exciton-Polariton Propagation. *Adv. Mater.* **2020**, *32*, 2002127. [CrossRef] [PubMed]
52. Amelines-Sarria, O.; dos Santos Claro, P.C.; Schilardi, P.L.; Blum, B.; Rubert, A.; Benitez, G.; Basiuk, V.A.; González Orive, A.; Hernández Creus, A.; Díaz, C.; et al. Electronic and magnetic properties of C60 thin films under ambient conditions: A multitechnique study. *Org. Electron.* **2011**, *12*, 1483–1492. [CrossRef]
53. Elschner, C.A.; Levin, A.; Wilde, L.; Grenzer, J.; Schroer, C.; Leo, K.; Riede, M. Determining the C60 molecular arrangement in thin films by means of X-ray diffraction. *J. Appl. Cryst.* **2011**, *44*, 983–990. [CrossRef]
54. Elsenbeck, D.K.; Das, S.; Velarde, L. Substrate influence on the interlayer electron–phonon couplings in fullerene films probed with doubly-resonant SFG spectroscopy. *Phys. Chem. Chem. Phys.* **2017**, *19*, 18519–18528. [CrossRef] [PubMed]

55. Huttner, A.; Breuer, T.; Witte, G. Controlling Interface Morphology and Layer Crystallinity in Organic Heterostructures: Microscopic View on C_{60} Island Formation on Pentacene Buffer Layers. *ACS Appl. Mater. Interfaces* **2019**, *11*, 35177–35184. [CrossRef] [PubMed]
56. Seydel, E.; Hoffmann-Vogel, R.; Marz, M. Epitaxial growth of C_{60} on highly oriented pyrolytic graphite surfaces studied at low temperatures. *Nanotechnology* **2019**, *30*, 025703. [CrossRef]
57. Oreshkina, A.I.; Bakhtizin, R.Z.; Sadowski, J.T.; Sakurai, T. Epitaxial Growth of C_{60} Thin Films on the Bi(0001)/Si(111) Surface. *Bull. Russ. Acad. Sci. Phys.* **2009**, *73*, 883. [CrossRef]
58. Bommel, S.; Kleppmann, N.; Weber, C.; Spranger, H.; Schafer, P.; Novak, J.; Roth, S.V.; Schreiber, F.; Klapp, S.H.L.; Kowarik, S. Unravelling the multilayer growth of the fullerene C60 in real time. *Nat. Commun.* **2014**, *5*, 5388. [CrossRef]
59. Acevedo, Y.M.; Cantrell, R.A.; Berard, P.G.; Koch, D.L.; Clancy, P. Multiscale Simulation and Modeling of Multilayer Heteroepitactic Growth of C_{60} on Pentacene. *Langmuir* **2016**, *32*, 3045–3056. [CrossRef]
60. Janke, W.; Speck, T. Modeling of epitaxial film growth of C60 revisited. *Phys. Rev. B* **2020**, *101*, 125427. [CrossRef]
61. Chen, L.; Wang, X.; Kumar, S. Thermal Transport in Fullerene Derivatives Using Molecular Dynamics Simulations. *Sci. Rep.* **2015**, *5*, 12763. [CrossRef] [PubMed]
62. Despoja, V.; Lončarić, I.; Mowbray, D.J.; Marušić, L. Quasiparticle spectra and excitons of organic molecules deposited on substrates: G0W0-BSE approach applied to benzene on graphene and metallic substrates. *Phys. Rev. B* **2013**, *88*, 235437. [CrossRef]
63. Tomaš, M.S. Green function for multilayers: Light scattering in planar cavities. *Phys. Rev. A* **1995**, 2545. [CrossRef] [PubMed]
64. Despoja, V.; Šunjić, M.; Marušić, L. Propagators and spectra of surface polaritons in metallic slabs: Effects of quantum-mechanical nonlocality. *Phys. Rev. B* **2009**, *80*, 075410. [CrossRef]
65. Novko, D.; Šunjić, M.; Despoja, V. Optical absorption and conductivity in quasi-two-dimensional crystals from first principles: Application to graphene. *Phys. Rev. B* **2016**, *93*, 125413. [CrossRef]
66. Despoja, V.; Mowbray, D.J. Using surface plasmonics to turn on fullerene's dark excitons. *Phys. Rev. B* **2014**, *89*, 195433. [CrossRef]
67. Rozzi, C.A.; Varsano, D.; Marini, A.; Gross, E.K.U.; Rubio, A. Exact Coulomb cutoff technique for supercell calculations. *Phys. Rev. B* **2006**, *73*, 205119. [CrossRef]
68. Despoja, V.; Jakovac, J.; Golenić, N.; Marušić, L. Bias-controlled plasmon switching in lithium-doped graphene on dielectric model Al2O3 substrate. *npj 2D Mater. Appl.* **2020**, *4*, 19. [CrossRef]
69. Giannozzi, P.; Baroni, S.; Bonini, N.; Calandra, M.; Car, R.; Cavazzoni, C.; Ceresoli, D.; Chiarotti, G.L.; Cococcioni, M.; Dabo, I.; et al. QUANTUM ESPRESSO: A modular and open-source software project for quantum simulations of materials. *J. Phys. Conden. Matter* **2009**, *21*, 395502. [CrossRef]
70. Troullier, N.; Martins, J.L. Efficient pseudopotentials for plane-wave calculations. *Phys. Rev. B* **1991**, *43*, 1993. [CrossRef]
71. Hamann, D.R. Optimized norm-conserving Vanderbilt pseudopotentials. *Phys. Rev. B* **2013**, *88*, 085117. [CrossRef]
72. Perdew, J.P.; Burke, K.; Ernzerhof, M. Generalized Gradient Approximation Made Simple. *Phys. Rev. Lett.* **1996**, *77*, 3865. [CrossRef] [PubMed]
73. Ong, Z.Y.; Fischetti, M.V. Charged impurity scattering in top-gated graphene nanostructures. *Phys. Rev. B* **2012**, *86*, 165422. [CrossRef]
74. Weaver, J.H.; Martins, J.L.; Komeda, T.; Chen, Y.; Ohno, T.R.; Kroll, G.H.; Troullier, N.; Haufler, R.E.; Smalley, R.E. Electronic structure of solid C60: Experiment and theory. *Phys. Rev. Lett.* **1991**, *66*, 1741. [CrossRef] [PubMed]
75. Lof, R.W.; van Veenendaal, M.A.; Koopmans, B.; Jonkman, H.T.; Sawatzky, G.A. Band gap, excitons, and Coulomb interaction in solid C60. *Phys. Rev. Lett.* **1992**, *68*, 3924. [CrossRef]
76. Sau, J.D.; Neaton, J.B.; Choi, H.J.; Louie, S.G.; Cohen, M.L. Electronic energy levels of weakly coupled nanostructures: C-60-metal interfaces. *Phys. Rev. Lett.* **2008**, *101*, 026804. [CrossRef]
77. Blase, X.; Attaccalite, C.; Olevano, V. First-principles GW calculations for fullerenes, porphyrins, phtalocyanine, and other molecules of interest for organic photovoltaic applications. *Phys. Rev. B* **2011**, *83*, 115103. [CrossRef]
78. Berkowitz, J. Sum rules and the photoabsorption cross sections of C_{60}. *J. Chem. Phys.* **1999**, *111*, 1446–1453. [CrossRef]
79. Lobanov, B.V.; Murzashev, A.I. Optical Absorption of Fullerene C_{60} Within the Concept of a Strongly Correlated State. *Russ. Phys. J.* **2016**, *59*, 856–861. [CrossRef]
80. Tiago, M.L.; Kent, P.R.C.; Hood, R.Q.; Reboredo, F.A. Neutral and charged excitations in carbon fullerenes from first-principles many-body theories. *J. Chem. Phys.* **2008**, *129*, 084311. [CrossRef]
81. Shnitov, V.V.; Mikoushkin, V.M.S.; Gordeev, Y. Fullerite C_{60} as electron-beam resist for 'dry' nanolithography. *Microelectron. Eng.* **2003**, *69*, 429–434. [CrossRef]
82. Shnitov, V.V.; Mikoushkin, V.M. Analysis of Fullerite C_{60} Electron Induced Modification in Terms of Effective Destruction Cross-section. *Fullerenes Nanotub. Carbon Nanostruct.* **2012**, *20*, 324–327. [CrossRef]
83. Nikolaev, A.V. Expansion of the pi-Molecular Orbitals of the C_{60} Fullerene in Spherical Harmonics. *Int. J. Quantum Chem.* **2011**, *111*, 2478–2481. [CrossRef]
84. Despoja, V.; Marušić, L. Use of surface plasmons for manipulation of organic molecule quasiparticles and optical properties. *J. Phys. Condens. Matter* **2014**, *26*, 485012. [CrossRef] [PubMed]